GDCh Research Article Angewandte International Edition Chemie www.angewandte.org

How to cite: *Angew. Chem. Int. Ed.* **2025**, *64*, e202414119
doi.org/10.1002/anie.202414119

Magnesium Batteries

Coupling Manipulation of Interfacial Chemistry and Coordination Structure in Vanadium Oxides Enables Rapid Magnesium Ion Diffusion Kinetics

*Weixiao Wang, Wenwen Wang, Fangyu Xiong, Jiashen Meng, Jinsong Wu, Wei Yang, Juncai Long, Jinghui Chen, Jiajun Chen, and Qinyou An**

Abstract: Rechargeable magnesium batteries (RMBs) are a highly promising energy storage system due to their high volumetric capacity and intrinsic safety. However, the practical development of RMBs is hindered by the sluggish Mg^{2+} diffusion kinetics, including at the cathode-electrolyte interface (CEI) and within the cathode bulk. Herein, we propose an efficient strategy to manipulate the interfacial chemistry and coordination structure in oligolayered V_2O_5 (L–V_2O_5) for achieving rapid Mg^{2+} diffusion kinetics. In terms of the interfacial chemistry, the specific exposed crystal planes in L–V_2O_5 possess strong electron donating ability, which helps to promote the degradation dynamics of C–F/C–S bonds in the electrolyte, thereby establishing the inorganic-organic interlocking CEI layer for rapid Mg^{2+} diffusion. In terms of the coordination structure, the straightened V–O structure in L–V_2O_5 provides efficient ions diffusion path for accelerating Mg^{2+} diffusion in the cathode. As a result, the L–V_2O_5 delivers a high reversible capacity (355.3 mA h g^{-1} at 0.1 A g^{-1}) and an excellent rate capability (161 mAh g^{-1} at 1 A g^{-1}). Impressively, the interdigital micro-RMBs is firstly assembled, exhibiting excellent flexibility and practicability. This work gives deeper insights into the interface and interior ions diffusion for developing high-kinetics RMBs.

Introduction

With the intense demands for increasing energy supply, the innovative energy storage technologies with higher energy/power density have received intensified pursuit.[1] Among them, rechargeable magnesium batteries (RMBs), as one of the most promising next-generation energy storage systems, have garnered substantial attention owing to their high volumetric specific capacity (3833 mAh cm^{-3}), low reduction potential (~2.37 V vs SHE), and abundant magnesium resources.[2] However, the development of viable RMBs are limited by sluggish Mg^{2+} diffusion kinetic in cathodes.[3] Particularly, unlike the monovalent carriers, the diffusion challenges of bivalent carriers are even pronounced owing to their inherently sluggish properties,[4] which results in large polarization resistance and low capacity storage efficiency.

Generally, the bottleneck of Mg^{2+} diffusion in cathodes is ascribed to sluggish Mg^{2+} transport at the cathode-electrolyte interface (CEI) and Mg^{2+} diffusion in the bulk materials.[5] The interfacial layer has a significant impact on the Mg^{2+} insertion from the liquid phase into the solid phase, which is a critical rate-limiting step during the electrochemical process.[6] However, the oligomers (e.g., polycarbonate) derived from incomplete decomposition of the electrolytes construct an ionically insulating CEI layer, which results in the large interfacial polarization.[7] In recent years, numerous efforts have been made to construct advanced CEI layers for achieving fast Mg^{2+} transport by promoting the dissociation of electrolyte, such as introducing strong chelating solvent and high electronegativity anions.[8] Although the modification of electrolytes can achieve fast Mg^{2+} transport at the interface of cathode, the Mg^{2+} diffusion in the bulk of cathode is still limited within the whole charge loop.[9] In terms of Mg^{2+} diffusion in the bulk materials, the dilemma is strong interactions between bivalent carriers and crystal structures.[10] To overcome the issues, some strategies have been proposed including expanding the interlayer distance by pre-intercalating foreign species,[11] introducing cationic/anionic heteroatoms,[12] and constructing cationic/anionic vacancies.[13] However, the above-mentioned methods involve minor structural modification for Mg^{2+} diffusion along the existing pathways, lacking the reconstruction of an entirely new high-speed ions diffusion pathways for maximal improvement.[14] To sum up, the simultaneous conducting interfacial chemistry and crystal engineering to maximally accelerate Mg^{2+} diffusion kinetics from the interface to the interior of the cathode is of great research significance, yet has not been reported.

In this work, we proposed an ultrathin V_2O_5 with specific exposed crystal planes and straightened V–O coordination structure for boosting the magnesium ion diffusion from the

[*] W. Wang, W. Wang, J. Meng, J. Wu, W. Yang, J. Long, J. Chen, J. Chen, Prof. Q. An
State Key Laboratory of Advanced Technology for Materials Synthesis and Processing,
Wuhan University of Technology, Wuhan 430070, China
E-mail: anqinyou86@whut.edu.cn
Prof. F. Xiong
College of Materials Science and Engineering, Chongqing University, Chongqing 400030, China

interface to the interior of the cathode, including at the cathode-electrolyte interface (CEI) and within the cathode bulk. In this case, the high surface electron density in the specific exposed crystal planes helps to promote the degradation of C–F/C–S bonds, thereby establishing the inorganic-organic interlocking CEI layer for rapid Mg^{2+} diffusion. In addition, the straightened V–O arrangement structure provides high-speed ions diffusion pathways for facilitating the Mg^{2+} diffusion kinetics within the interlayer of V_2O_5. In terms of the interfacial chemistry, we have performed the two-dimensional grazing incidence wide-angle X-ray scattering (GIWAXS) patterns in L–V_2O_5 electrode to prove specific exposed crystal planes distribution. And the time-of-flight secondary-ion mass spectrometry (TOF-SIMS) shows that an inorganic-organic interlocking CEI layer are formed for supporting fast Mg^{2+} diffusion at the interface of the cathode. In terms of the coordination structure, the structural reconstruction in the L–V_2O_5 were investigated by X-ray absorption near-edge structure (XANES). It is worth noting that the interdigital micro-MRBs is firstly assembled, demonstrating excellent practicability and flexibility. This work provides a promising strategy to simultaneously boost Mg^{2+} diffusion kinetics at the interface and in the bulks of cathodes.

Results and Discussion

The Mg^{2+} diffusion kinetics in cathodes depends heavily on the Mg^{2+} transport at the cathode-electrolyte interface (Step I) and Mg^{2+} diffusion in the bulk materials (Step II). As shown in Figure 1a, the low surface electron density in bulk V_2O_5 (B–V_2O_5) impacts the incomplete decomposition of the bis (trifluoromethanesulfonyl) imide anions ($TFSI^-$) in electrolyte, leadings to the formation of oligomers-dominated CEI layer. Consequently, the CEI layer decelerates the Mg^{2+} diffusion kinetics at the cathode-electrolyte interface (Step I). Besides, the B–V_2O_5 is formed by [VO_5] square pyramids, which are intensely distorted interconnected through shared edges and vertices in the ab plane (Figure S1a).[15] The zigzag V–O coordination structure impedes Mg^{2+} diffusion in the bulk materials (Step II).[16] To overcome the aforementioned issues, we proposed the hydroxylation and condensation strategy to achieve the rearrangement and reconstruction of crystal structure (Figure S2, S3). First, the hydrogenation reaction converts the four-coordination structure of V atoms into six-coordination structure. Second, the condensation reaction encompasses the olation and oxolation process, resulting in the formation of the bilayers V_2O_5.

The obtained oligolayered V_2O_5 (L–V_2O_5) processes high surface electron density and straightened V–O coordination structure, which synergistically boosts the Mg^{2+} diffusion kinetics from the interface to the interior of the cathode (Figure 1b). In detail, the specific exposed crystal plane in L–V_2O_5 with high surface electron density helps to promote the degradation dynamics of C–F/C–S bonds in the electrolyte, thereby establishing the inorganic-organic interlocking CEI layer for rapid Mg^{2+} diffusion (Step I). Besides, the straightened O–V structure provides efficient ions diffusion path for speeding up Mg^{2+} diffusion kinetics within the framework (Step II). Moreover, introducing crystal water and expanded interlayer spacing in L–V_2O_5 also weaken the electrostatic interaction

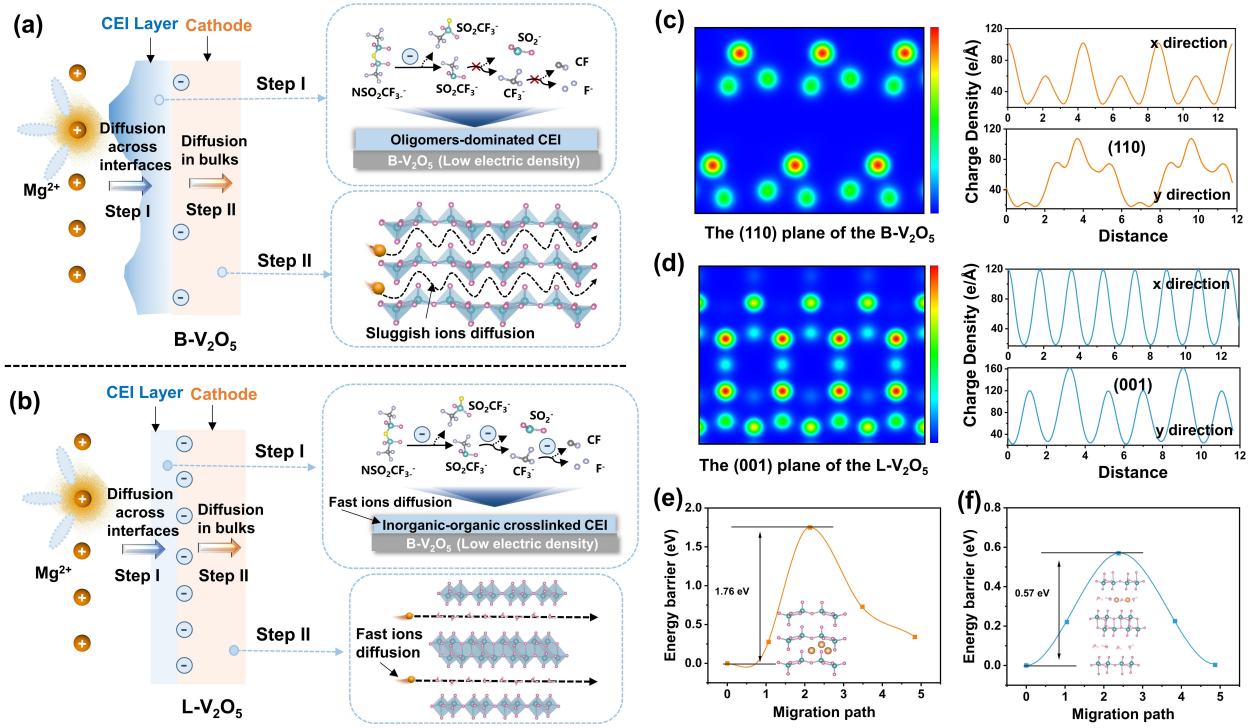

Figure 1. Schematic illustration of the Mg^{2+} diffusion during the electrode-electrolyte interface and bulk materials in a) B–V_2O_5, and b) L–V_2O_5 cathode. c, d) Charge density distributions of exposed crystal planes and e, f) Mg^{2+} migration behaviors in B–V_2O_5 and L–V_2O_5 cathode.

between divalent Mg^{2+} and host materials, facilitating the Mg^{2+} diffusion kinetics. In addition, we have performed the GIWAXS patterns of B–V_2O_5 and L–V_2O_5 electrodes to explore the crystal planes distribution on the surface of electrodes (Figure S4). The results indicate that (001) crystal plane are primarily presented on the L–V_2O_5 electrode, and the (110) crystal plane has a relatively high distribution on the B–V_2O_5 electrode. As a reference, the exposed crystal (001) plane of L–V_2O_5 displays a higher surface electron density compared to the (110) plane of B–V_2O_5 by density functional theory (DFT) calculation (Figure 1c, d). Besides, as shown in Figure 1e, f, the calculated Mg^{2+} diffusion barrier of L–V_2O_5 (0.57 eV) is much lower than B–V_2O_5 (1.76 eV) along the interlayer directions of crystal. To sum up, synergistically boosting ion diffusion kinetics from the interface to the interior in L–V_2O_5 is essential for achieving high-kinetics RMBs.

The scanning electron microscopy (SEM) image (Figure 2a) of L–V_2O_5 shows ultrathin and giant nanosheets, in which some ridges and folds structure associated with the deformation and wrinkling of ultrathin nanosheets. In addition, the transmission electron microscopy (TEM) image (inset in Figure 2a, Figure S5) shows that the L–V_2O_5 features ultrathin nanosheets with semi-transparent. The high-resolution transmission electron microscope (HRTEM) image of L–V_2O_5 was obtained by cryo-electron microscopy, displays well-defined lattice fringes with a lattice space of ~0.38 nm (Figure 2b). Furthermore, the thickness of the layered V_2O_5 is detected to be ~2.18 nm by atomic force microscopy (AFM) measurement, corresponding to two layers VO_6 octahedra after structural reconstruction (Figure 2c). The TEM images and AFM images from other parts of the samples are further provided in Figure S6. In addition, the digital photographs of the flexible L–V_2O_5 film are displayed in Figure S7. As a contrast, the detailed structural characterization of B–V_2O_5 is shown in Figure S8. In Figure 2d, X-ray diffraction (XRD) patterns exhibits that the B–V_2O_5 (JCPDS No. 41–1426) has converted to L–V_2O_5 (JCPDS No. 40–1296).[17] The L–V_2O_5 displays the broad and weak (001) peak, indicating that L–V_2O_5 is very thin along the c-direction. In addition, the diffraction peeks of the (001) plane, (003) plane, (004) plane and (005) plane in the XRD pattern of L–V_2O_5 all belong to the (001) crystal planes. Furthermore, the powder XRD Rietveld refinement illustrates the L–V_2O_5 have lattice parameters of a = 14.12 Å, b = 4.11 Å, c = 11.19 Å, α = γ = 90°, and β = 86.078°in the space group of C2/m, which further indicates the reconstruction of the V–O coordination structure (Figure S9, Table S1, S2). The structure information of B–V_2O_5 and L–V_2O_5 is further exhibited by Raman spectra (Figure S10). In contrast to the B–V_2O_5, the V–O–V and V=O bonds of L–V_2O_5 undergo

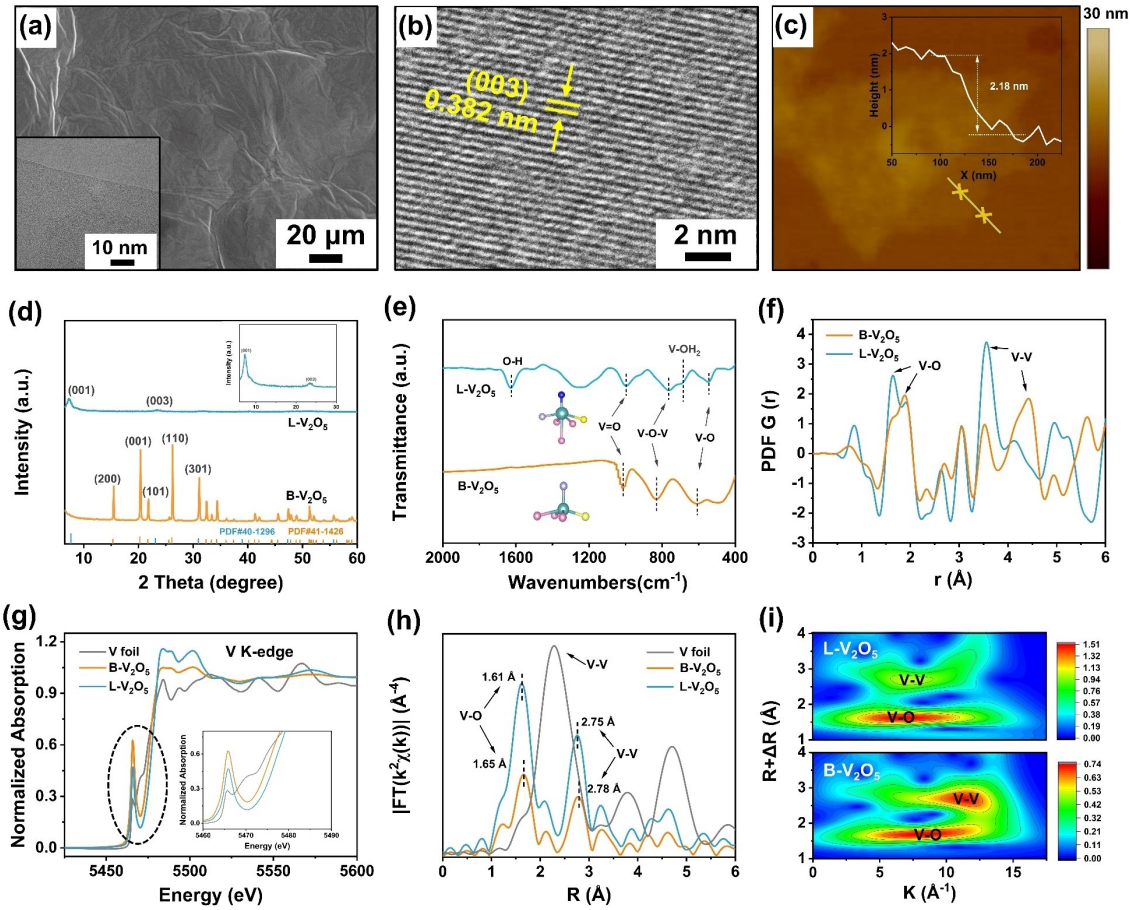

Figure 2. a) SEM image and TEM image, b) HRTEM image, and c) AFM image of L–V_2O_5. d) XRD patterns, e) FTIR spectra, and f) PDF curves of B–V_2O_5 and L–V_2O_5. g) The normalized V K-edge XANES spectra, and h) V K-edge EXAFS spectra of B–V_2O_5, L–V_2O_5, and V foil. i) WT-EXAFS spectra of B–V_2O_5 and L–V_2O_5.

shifts, attributed to the variation of the bond lengths/angles after structural reconstruction.[18] In the Fourier transform infrared spectroscopy (FTIR) spectra, the peaks at 1012, 829, and 607 cm^{-1} in B–V_2O_5 are assigned to the V=O/V–O–V stretching vibration, and V–O bending vibration, respectively (Figure 2e).[19] Compared to the B–V_2O_5, the peaks of L–V_2O_5 shifts slightly toward lower wavenumbers, which are attributed to the modification of V–O coordination structure. The thermogravimetric analysis (TG) further verifies the existence of crystal water in Figure S11. The element compositions of B–V_2O_5 and L–V_2O_5 were explored by X-ray photoelectron spectroscopy (XPS) (Figure S12).[20] To obtain the structural environment of B–V_2O_5 and L–V_2O_5, the PDF analyses were implemented (Figure 2f, S13). The peaks (V–O/V–V) are shifted, which is associated with the slippage of V–O band. Moreover, based on the structural model of the space group Pmmn of V_2O_5, the chemical formula of B–V_2O_5 was fitted as orthorhombic V_2O_5 (Figure S14). In agreement with the EXAFS analyses, X-ray absorption near-edge structure (XANES) and extended X-ray absorption fine structure (EXAFS) were employed to further reveal the structure characteristics of B–V_2O_5 and L–V_2O_5. In Figure 2g, compared with the B–V_2O_5, the adsorption edge of L–V_2O_5 shifts to a higher binding energy, indicates the existence of abundant valent state of V^{5+} (Figure S15). In addition, the intensity of the pre-edge peak (dipole-forbidden peak, 1 s→3d) in the L–V_2O_5 significantly decreases, which are related to the formation of tetrahedral and octahedral VO_x sites due to the distorted square-pyramidal bonding in V_2O_5.[21] The Fourier-transformed (FT) and wavelet-transformed (WT) EXAFS spectra (Figure 2h, i, S16) exhibits the structural reconstruction in V–O and V–V coordination. The peaks at 1.65 Å (V–O) and 2.78 Å (V–V) in B–V_2O_5 are shifted to 1.61 Å and 2.75 Å in L–V_2O_5, which further verifies the transformation of bond lengths/angles after structural reconstruction.

The CEI layer on the cathode surface plays a pivotal role in governing ionic transfer during the electrochemical reactions process. The chemical composition of CEI layer was investigated by XPS measurement along with the etching the percentage of CEI thickness. In the F 1s spectra (Figure 3a), there are two peaks of CF_3 and MgF_2 species, which are derived from the PVDF binder and the decomposition product of $TFSI^-$. After Ar^+ etching treatment, the peaks of MgF_2 species in B–V_2O_5 electrode gradually increase, which indicates the uneven distribution of MgF_2 throughout the whole depth of the thick CEI layer. In comparison, the peak of MgF_2 in L–V_2O_5 electrode remain unchanged after etching the 20 % and 40 % of CEI thickness, which are attributed to the inorganic-organic interlocking CEI layer. The peak of MgF_2 species nearly disappears after etching 100 % of CEI thickness. In the O 1s spectra (Figure 3b), the peaks assigned to the C–O and V–O originate from the decomposition of the electrolyte and vanadium oxide.[23] Compared with B–V_2O_5 electrode, the peak of V–O bond in L–V_2O_5 electrode is very slight after etching the 20 % and 40 % of CEI thickness, which indicates that the CEI layer helps to suppress the dissolution of vanadium oxides during charging and discharging process. In addition, the XPS survey spectra of B–V_2O_5 and L–V_2O_5 electrode are shown in Figure S17. The HRTEM image shows that the thickness of

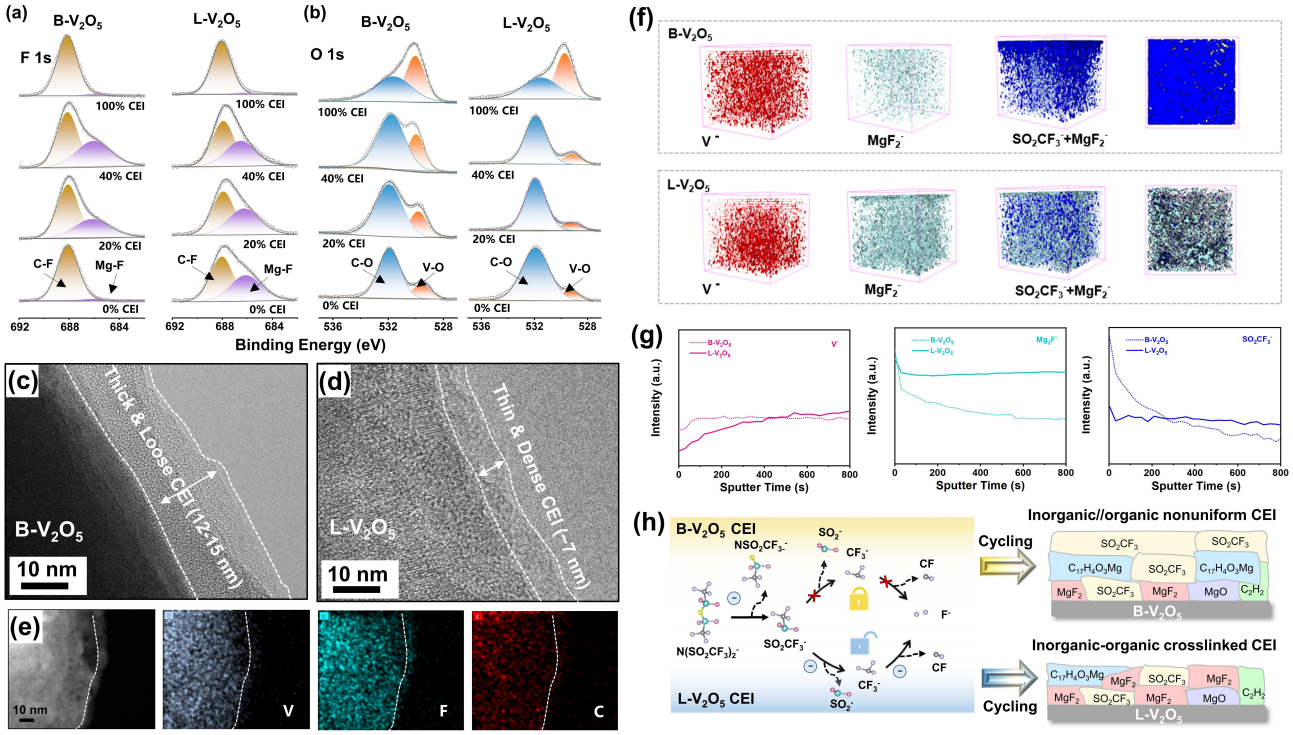

Figure 3. a) In-depth F 1s XPS spectra, and b) O 1s XPS spectra of electrodes. TEM images of c) B–V_2O_5, and d) L–V_2O_5 cathodes. e) STEM-EDS mappings of L–V_2O_5 electrode. f) The 3D views, and g) the corresponding depth profiles of electrolyte decomposition species in the TOF-SIMS sputtered volume of cathodes. h) Schematic diagram of the structural evolution of CEI layer in B–V_2O_5 and L–V_2O_5 cathodes.

CEI layer in B–V_2O_5 electrode is 12–15 nm (Figure 3c). In contrast, a thin CEI layer with a thickness of ~7 nm was observed in the L–V_2O_5 electrode (Figure 3d, S18). Furthermore, STEM-EDS images of B–V_2O_5 and L–V_2O_5 electrodes further directly verifies the existence of F, C and Mg elements on the CEI layer (Figure 3e, Figure S19, S20). Notably, the CEI layer of L–V_2O_5 electrode exhibits a uniform distribution of F and C elements, exhibiting that the specific exposed crystal plane in L–V_2O_5 electrode facilitates the formation of inorganic-organic interlocking and thin CEI layer. The time-of-flight secondary ion mass spectrometry (TOF-SIMS) has been applied to analyze the ionic fragments of CEI components (Figure 3f and Figure S21). In the B–V_2O_5 electrode, substantial $SO_2CF_3^-$ ionic fragments are primarily accumulated in the outermost layer of the CEI, while limited MgF_2^- ionic fragments are distributed in the inner layer, which are testified in the top-down view of $SO_2CF_3^-$ and MgF_2^- ionic fragments. On the contrary, both $SO_2CF_3^-$ and MgF_2^- are uniformly distributed throughout the CEI layer in L–V_2O_5 electrode, exhibiting an inorganic-organic interlocking distribution structure. As a reference, the decomposition mechanism of $Mg(TFSI)_2$ can be described as follows (Figure S22):[24]

$$N(SO_2CF_3)_2^- + e^- \rightarrow NSO_2CF_3^- + SO_2CF_3^- \quad (1)$$

$$SO_2CF_3^- + e^- \rightarrow SO_2^- + CF_3^- \quad (2)$$

$$CF_3^- + e^- \rightarrow CF + 2F^- \quad (3)$$

$$2F^- + Mg^{2+} \rightarrow MgF_2 \quad (4)$$

Therefore, the inorganic-organic interlocking CEI structure in L–V_2O_5 is primarily attributed to the high surface electron density in the specific exposed crystal plane, which is beneficial for catalyzing the adequate decomposition of $TFSI^-$. And the AN solvent rarely decomposes on the surface of L–V_2O_5 during cycling (Figure S23). Moreover, in contrast to B–V_2O_5, the surface layer of L–V_2O_5 exhibits a lower concentration of V^- ionic fragments, suggesting a lesser dissolution of transition metal ions (Figure S24). The primary reason is that the surface adsorption-intercalation storage mechanism of L–V_2O_5 avoids the lattice spacing repeated expansion and contraction during continuous ions (de) intercalation. Figure 3g depict the depth profiling data of V^-, $SO_2CF_3^-$, and MgF_2^- species in the B–V_2O_5 and L–V_2O_5 electrodes. These data exhibit the same distribution trend as presented in the depth 3D and 2D distribution map. The structure and component of CEI layer is formed through an interface-confined locking or unlocking process, which initiates or hinders the adequate decomposition of $TFSI^-$, derived from the surface electron density in the main exposed crystal plane of V_2O_5 electrode (Figure 3h, S25). As a result, the B–V_2O_5 electrode exhibits oligomers-dominated CEI layer, while the L–V_2O_5 electrode features an inorganic-organic interlocking CEI layer for rapid and stable Mg^{2+} diffusion.

To further understand the impact of interfacial chemistry and bulk engineering on the Mg^{2+} diffusion, the half-cell was assembled using activated carbon cloth (AC) as counter electrode, L–V_2O_5 as cathode, and 0.3 M $Mg(TFSI)_2$/AN as the electrolyte. Figure 4a shows the typical cyclic voltammetry (CV) profiles for B–V_2O_5 and L–V_2O_5 electrodes with a potential window of −1.1–1.4 V at 0.5 mV s^{-1}. Compared with the B–V_2O_5, the extra pair of redox/reduce peaks in L–V_2O_5 originates from the further reduction reaction of the V^{3+}/V^{4+} redox couples (Figures S26, S27). The CV curves of L–V_2O_5 and B–V_2O_5 electrodes at different scan rate are depicted in Figures S28. Based on the CV profiles, the electrochemical kinetics can be further analyzed through the function of $i = av^b$, where a and b are variable parameters, i is the peak current, and v is the scan rate.[25] Figure 4b displays the b-values derived from the slopes of log (i) versus log (v). Compared with the B–V_2O_5, b-values in L–V_2O_5 are significantly closer to 1, suggesting that the electrochemical reaction in the L–V_2O_5 electrode is almost capacitive behavior. In addition, the SSA of L–V_2O_5 is 60.21 $m^2 g^{-1}$ (Figure S29), which indicates negligible EDLC to the total measured capacity. Therefore, the pseudocapacitive dominated storage behavior occurs in the L–V_2O_5. In Figure 4c, the defined plateaus in the galvanostatic charge/discharge (GCD) profiles are well corresponded to the CV peaks. The L–V_2O_5 electrode delivers a high reversible discharge capacity of 355.3 mAh g^{-1}, which significantly stands out among those of the vanadium-based electrodes for magnesium battery (Table S3). The water contents are 118 ppm in 0.3 M $Mg(TFSI)_2$/AN, which demonstrates a minor capacity contribution of proton intercalation in the L–V_2O_5. Impressively, the L–V_2O_5 electrode maintains a high discharge capacity of 256.6 mAh g^{-1} after 100 cycles, which far surpasses that of the B–V_2O_5 electrode (Figure 4d). The charge/discharge curves at different cycles of B–V_2O_5 and L–V_2O_5 electrode are shown in Figure S30. The diffusion coefficient of Mg^{2+} (D_{Mg}) in L–V_2O_5 electrode was determined using galvanostatic intermittent titration technique (GITT) in Figure 4e, S31. The obtained results indicate that D_{Mg} magnitude ranges from 8.42×10^{-11} to 4.27×10^{-13} $cm^2 s^{-1}$, which is significantly higher than that of the B–V_2O_5 electrode (Figures S32). The L–V_2O_5 exhibits the fast Mg^{2+} diffusion kinetics during the decoupling of bulk engineering and interfacial chemistry, and the D_{Mg} values is higher than that of the reported vanadium oxides electrodes for RMBs (Table S4). Compared with B–V_2O_5 electrode, the L–V_2O_5 electrode delivers a high reversible specific capacity of 347.2, 300.4, 235.7, 192.2, and 161 mAh g^{-1} at the current density 0.05, 0.1, 0.2, 0.5, and 1 A g^{-1}, respectively (Figure 4f, S33). Remarkably, the specific capacity of the L–V_2O_5 electrode mostly returned to 299.7 mAh g^{-1} at 0.1 A g^{-1}, signifying the excellent rate performance. According to the Nyquist plots and fitting results (Figure 4g), the L–V_2O_5 electrode shows smaller Warburg coefficients ($\sigma = 28.21$) than those of the B–V_2O_5 electrode ($\sigma = 68.73$, which further confirms the improved Mg^{2+} diffusion kinetics in L–V_2O_5 electrode. In addition, the L–V_2O_5 electrode exhibits a smaller R_{ct} value (16.58 Ω) compared to the B–V_2O_5 electrode (20.64 Ω) (Figure S34). To explore the simultaneous improvement of Mg^{2+} diffusion from the interface to the interior of the cathode, we tested the electrochemical impedance spectroscopies (EIS) of B–V_2O_5 and L–V_2O_5 electrode after 30 cycles, and analyzed the data using the relaxation time semi-quantitative distribution (DRT) method (Figure 4h). The four major peaks (labeled C1, C2, C3, and C4) in the DRT diagram is related to the Mg^{2+} diffusion across the CEI layer (C1, C2, and C3), and Mg^{2+}solid-state diffusion in electrodes (C4). In

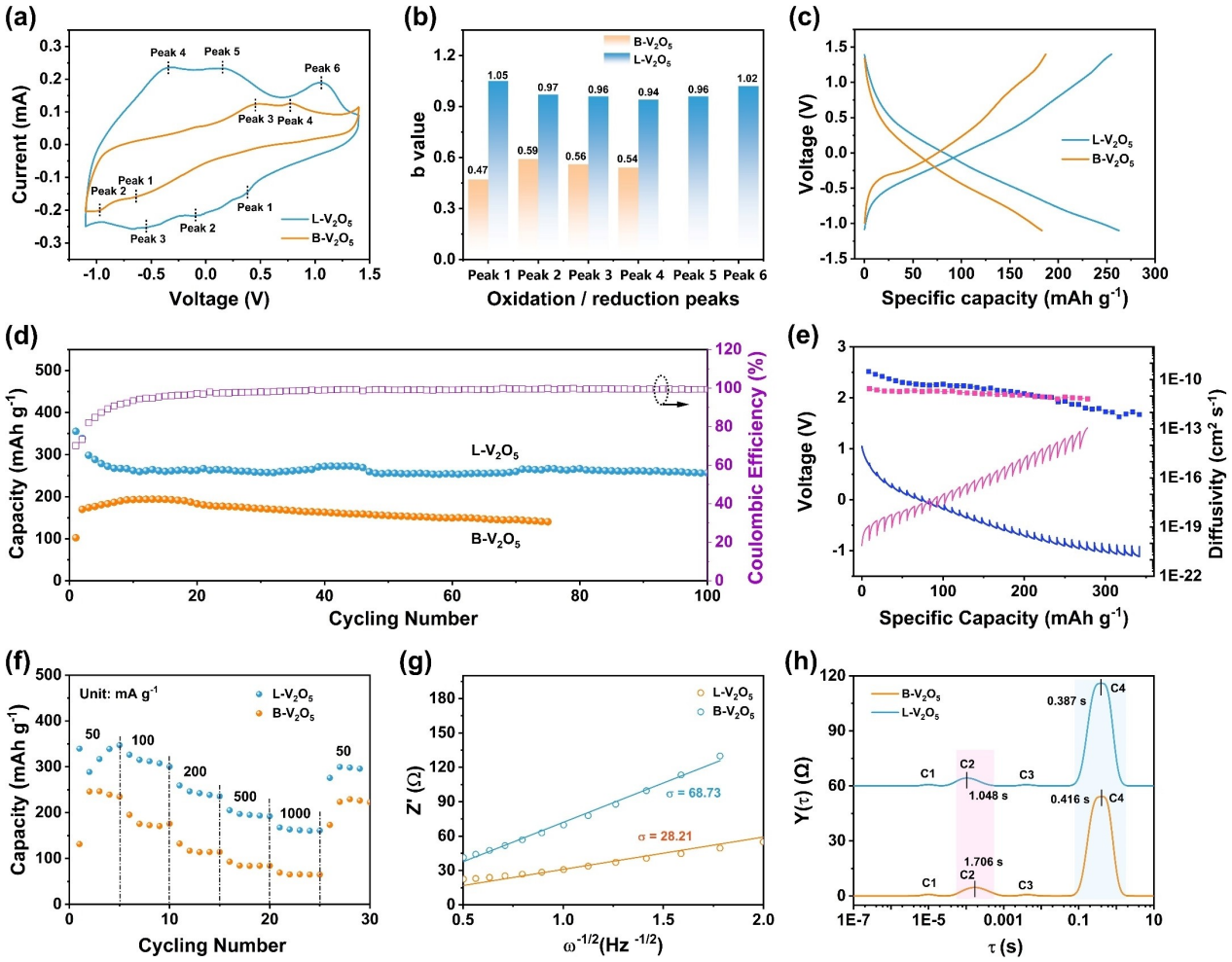

Figure 4. a, b) CV curves and the corresponding calculated b values, c) GCD curves, and d) cycling performances of B–V_2O_5 and L–V_2O_5 electrode. e) GITT curves and the calculated Mg^{2+} diffusion coefficients of L–V_2O_5 electrode. f) Rate capability at 0.05–1 $A g^{-1}$, g) impedance spectra and the relationship between Z′ and $w^{-1/2}$ ($w = 2\pi f$), and h) DRT calculated from impedance spectra of B–V_2O_5 and L–V_2O_5 electrode.

contrast to B–V_2O_5, the time constants of C2 and C4 in the L–V_2O_5 electrode exhibit lower values, which indicates the simultaneous improvement of Mg^{2+} transport at the cathode-electrolyte interface (CEI) and Mg^{2+} diffusion in the bulk materials. Furthermore, the thickness of materials significantly also affects their electrochemical performance, which is attributed to the reduced particle size and abundant exposed crystal planes (Figure S35).

To investigate the energy storage mechanism of L–V_2O_5 electrode, the in situ Raman, in situ XRD, in situ EIS and ex situ XPS measurement were performed. In in situ Raman spectra (Figure 5a), the main peaks at 152 cm^{-1} (V–O–V bonds), 256 cm^{-1} (O_3–V=O bonds), 347 cm^{-1} (V–O_3–V bonds), 505 cm^{-1} (V–O_2–V bonds) and 702 cm^{-1} (V_2–O bonds) gradually decrease and then recover during discharge/charge processes, which also clearly observed in Raman diagrams (Figure S36, S37). The results indicate that V–O bonds are broken and reconnected by Mg^{2+} insertion and extraction. As depicted in the in situ XRD patterns (Figure 5b), the diffraction peaks of (001), (003), and (005) are barely shifted during the charge/discharge processes, indicating the excellent structural stability of L–V_2O_5. In contrast, the incompletely recovered (001) peak position in B–V_2O_5 electrode manifests that the zigzag V–O coordination structure impedes Mg^{2+} de-intercalation and diffusion (Figure S38). In Figure S39, the chemical state evolution of L–V_2O_5 electrodes at different states was also observed by XPS spectra. For the pristine electrode, the peaks at 524.8 and 517.4 eV are indexed to the signal of V^{5+}. Upon discharging to −1 V, two pairs of new peaks emerge at lower binding energies (522.3/514.8 eV and 523.6/516.2 eV), which are corresponded to the signals of V^{3+} and V^{4+}.[26] Moreover, the proportion of V^{3+} obviously increases, while the V^{5+} is correspondingly diminished with deeper discharging. Upon charging to 1.4 V, the electrode reverts to the pristine state with no residual V^{3+} states, reflecting its superior reversibility. The discharge/charge curve with selected points of the L–V_2O_5 electrode and the corresponding proportion ratio of V^{3+}, V^{4+}, and V^{5+} are shown in Figure 5c. In situ EIS test of L–V_2O_5 electrode was also carried out at various charge/discharge states to conduct in-depth kinetic investigations (Figure 5d). During the discharging, the decrease in R_{ct} values could be attributed to the formation of V^{4+} and the insertion of Mg^{2+}.

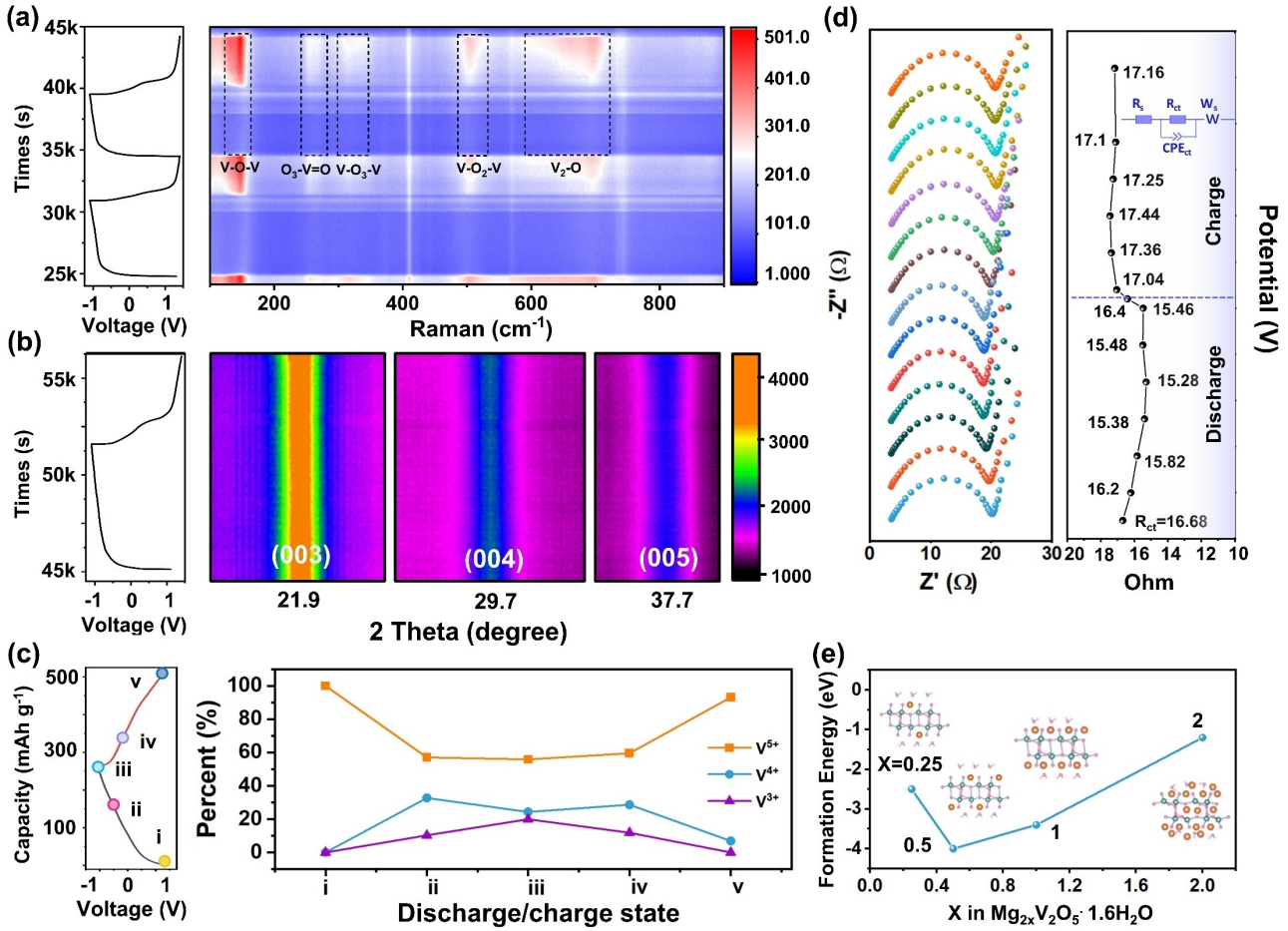

Figure 5. a) in situ 2D Raman spectra, b) in situ XRD patterns, c) ex situ V 3d XPS spectra, and d) in situ Nyquist plots and the corresponding fitting parameter (R_{ct}) of L–V_2O_5 electrode at various discharged and charged states. e) Crystal structure models and the corresponding formation energy of monolayer $Mg_{2x}V_2O_5 \cdot 1.6H_2O$.

During the charging, the continual increase in resistances is ascribed to the reversible extraction of Mg^{2+}, emphasizing the reversibility of the L–V_2O_5 electrode. As shown in Figure 5e and S40, the density functional theory (DFT) calculates indicates that, unlike the traditional ion insertion-type storage mechanism of B–V_2O_5, the energy storage mechanism of L–V_2O_5 is predominantly characterized by ions adsorption-insertion behavior.

To verify the feasibility of L–V_2O_5 electrode for practical applications, we constructed a full cell and microdevice, using L–V_2O_5 as cathode, ultrathin Mg metal as anode, and magnesium trifluoromethanesulfonate based salts (MTB) as electrolyte (Figure 6a). In Figure 6b, the full cell exhibits high capacity of 157.1 mAh g^{-1} at 0.1 A g^{-1}, which exhibits highly competitive in multivalent-ion batteries. In Figure 6c, the rate performance of the full cell delivers a high reversible specific capacity of 119.3, 111.3, 83.6, 62.6, and 43.1 mAh g^{-1} at the current density 0.1, 0.2, 0.5, 1, and 2 A g^{-1}, respectively. Remarkably, the specific capacity of the full cell mostly returned to 129.9 mA h g^{-1} at 0.1 A g^{-1}, signifying the high-rate tolerance. As a contrast, cycling performances and rate capability of B–V_2O_5 electrode are shown in Figure S41. As a demo, the L–V_2O_5 coated on the carbon paper and magnesium foil are accurately fabricated into interdigital microelectrodes based on a pre-designed pattern. Then, the L–V_2O_5 cathode and Mg anode are correspondingly adhered into the polyimide tape to assemble into flexible interdigital micro-MRBs (Figure 6d, e, S42). As expected, a single interdigital micro-MRBs can adequately power the timer (Figure 6f), which validates that the interdigital microdevice is an excellent micro-power-source with high energy density. In Figure 6g, the GCD curves of a single micro-MRBs exhibits a high area specific capacity of 0.139 mAh cm^{-2} at the current density 1 mA cm^{-2}. More impressively, a single micro-MRBs can adequately power the sensor for capturing each rhythm of the pressure, which exhibits the excellent practicability and flexibility.

Conclusions

In this research, we designed atomically thin V_2O_5 cathode with specific exposed crystal planes and straightened V–O coordination structure via structural reconstruction, synergistically boosting the Mg^{2+} diffusion kinetics from the interface to the interior of the cathode. Especially, the specific exposed crystal planes in the L–V_2O_5 helps to promote the degradation of C–F/C–S

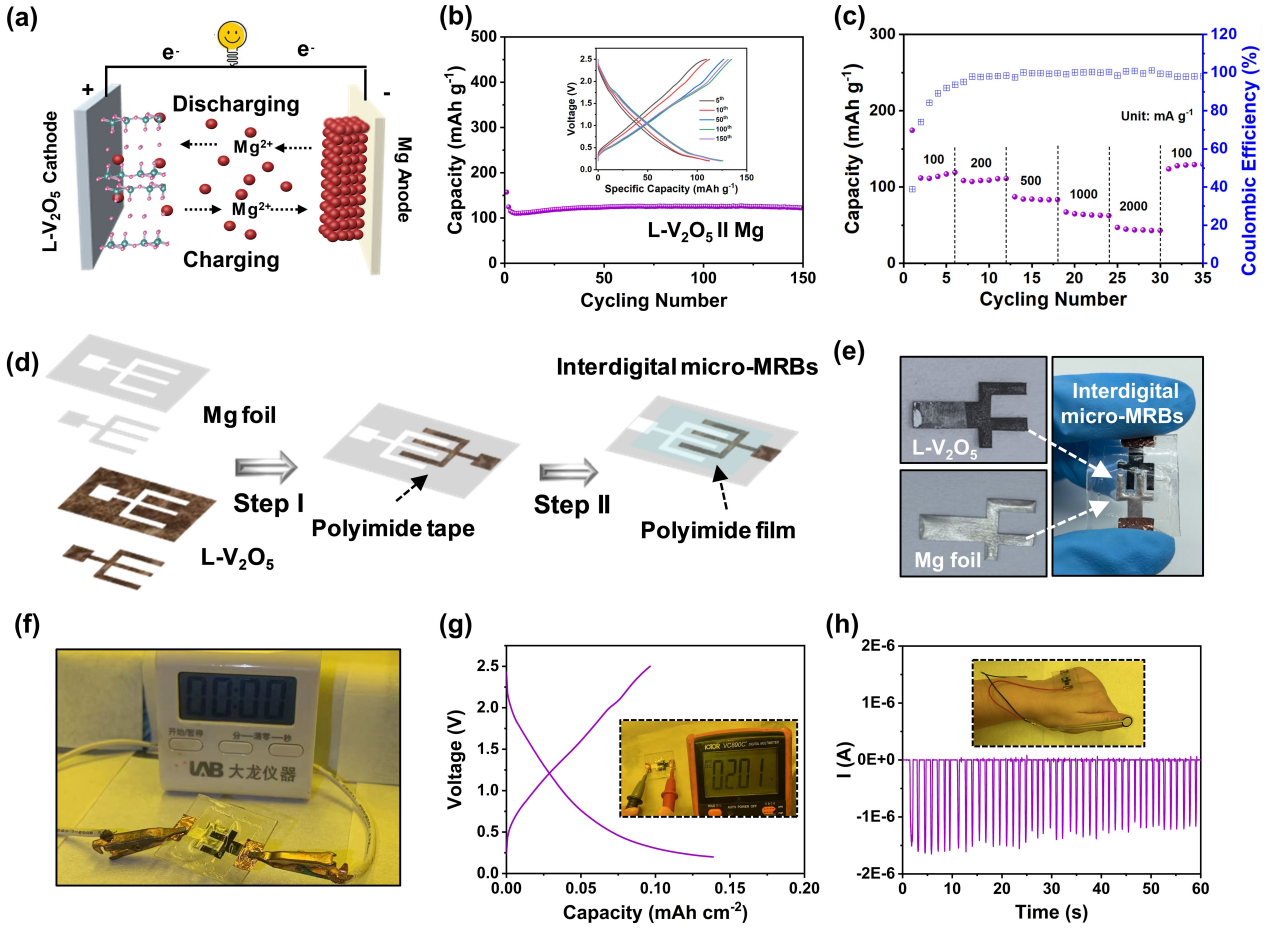

Figure 6. a) Schematic illustration of the assembled L–V_2O_5//Mg full cell. b) Cycling performances, and c) rate performances of the full cell. d) Schematic diagram of the fabrication process of interdigital micro-MRBs. Photographs of e) the Mg anode, L–V_2O_5 cathode and interdigital micro-MRBs. f) Photographs of the timer powered by a single microdevice. g) GCD curves of a single microdevice. h) The i-t curves of pressure sensor powered by a single microdevice.

bonds, establishing the inorganic-organic interlocking CEI layer for rapid Mg^{2+} diffusion. In addition, the straightened V–O arrangement structure provides high-speed ions diffusion pathways for facilitating the Mg^{2+} diffusion kinetics within the bulk of L–V_2O_5. The designed V_2O_5 delivers a high reversible capacity (355.3 mA h g^{-1} at 0.1 A g^{-1}), and an excellent rate capability (161 mAh g^{-1} at 1 A g^{-1}). Further, the interdigital micro-MRBs unveils extraordinary practicability and excellent flexibility. This work provides fundamental insights into the synergistically boosting the Mg^{2+} diffusion kinetics from the interface to the interior of the cathode, which may be applicable to other multivalent ion battery systems.

Supporting Information

The Supporting Information is available free of charge.

Acknowledgements

This work was supported by the National Key Research and Development Program of China [2023YFB3809501]; National Natural Science Foundation of China [Nos. 52172231, 52127816, 51972259, and 52202290]; National Energy-Saving and Low-Carbon Materials Production and Application Demonstration Platform Program [TC220H06 N]; and The Natural Science Foundation of Hubei Province (2022CFA087), Key Research and Development Program of Hubei (2022BAA027). We would like to acknowledge the Synchrotron Light Research Institute (Public Organization, SLRI) for provision of beamtime. We appreciate Dr. Suttipong Wannapaiboon and the staff of beamline 1.1 W for their assistance.

Conflict of Interest

The authors declare no conflict of interest.

Data Availability Statement

The data that support the findings of this study are available from the corresponding author upon reasonable request.

Keywords: Rechargeable magnesium batteries · Interfacial chemistry · Atomically thin vanadium oxide · Interdigital microdevices

[1] a) Q. K. Zhang, X. Q. Zhang, J. Wan, N. Yao, T. L. Song, J. Xie, L. P. Hou, M. Y. Zhou, X. Chen, B. Q. Li, R. Wen, H. J. Peng, Q. Zhang, J. Q. Huang, *Nat. Energy* **2023**, *8*, 725; b) H. C. Xia, L. X. Zan, P. F. Yuan, G. Qu, H. L. Dong, Y. F. Wei, Y. Yu, Z. Y. Wei, W. F. Yan, J. S. Hu, D. H. Deng, J. N. Zhang, *Angew. Chem. Int. Ed.* **2023**, *62*, e202218282; c) Y. H. Zhu, J. Z. Wang, Q. Zhang, Y. F. Cui, G. Huang, J. M. Yan, X. B. Zhang, *Energy Environ. Sci.* **2022**, *15*, 1529.

[2] a) Z. Y. Li, J. Häcker, M. Fichtner, Z. Zhao-Karger, *Adv. Energy Mater.* **2023**, *13*, 2300682; b) J. C. Long, S. S. Tan, J. J. Wang, F. Y. Xiong, L. M. Cui, Q. Y. An, L. Q. Mai, *Angew. Chem. Int. Ed.* **2023**, *62*, e202301934.

[3] a) D. M. Wang, X. F. Du, G. S. Chen, F. C. Song, J. H. Du, J. W. Zhao, Y. L. Ma, J. Wang, A. Du, Z. L. Cui, X. H. Zhou, G. L. Cui, *Angew. Chem. Int. Ed.* **2023**, *62*, e202217709; b) W. X. Wang, Y. L. Jiang, Y. Yang, F. Y. Xiong, S. H. Zhu, J. J. Wang, L. L. Du, J. H. Chen, L. M. Cui, J. Xie, Q. Y. An, L. Q. Mai, *ACS Nano* **2022**, *16*, 17097.

[4] a) Z. Y. Li, J. Häcker, M. Fichtner, Z. Zhao-Karger, *Adv. Energy Mater.* **2023**, *13*, 2300682; b) X. Zhang, D. Li, Q. Ruan, L. Liu, B. Wang, F. Xiong, C. Huang, P. K. Chu, *Mater. Today Energy* **2023**, *32*, 101232.

[5] M. Huang, X. P. Wang, J. J. Wang, J. S. Meng, X. Liu, Q. He, L. S. Geng, Q. Y. An, J. L. Yang, L. Q. Mai, *Angew. Chem. Int. Ed.* **2023**, *62*, e202308961.

[6] Y. L. Shen, Y. J. Wang, Y. C. Miao, Q. Li, X. Y. Zhao, X. D. Shen, *Adv. Mater.* **2023**, *35*, 2208289.

[7] a) H. B. Dong, R. R. Liu, X. Y. Hu, F. J. Zhao, L. Q. Kang, L. X. Liu, J. W. Li, Y. S. Tan, Y. Q. Zhou, D. J. L. Brett, G. J. He, I. P. Parkin, *Adv. Sci.* **2022**, *10*, 2205084; b) Y. L. Yang, H. P. Wang, C. L. Zhu, J. M. Ma, *Angew. Chem. Int. Ed.* **2023**, *62*, e202300057; c) Z. W. Zhang, J. L. Yang, W. Huang, H. S. Wang, W. J. Zhou, Y. B. Li, Y. Z. Li, J. W. Xu, W. X. Huang, W. Chiu, Y. Cui, *Matter* **2021**, *4*, 302.

[8] a) Y. H. Man, P. Jaumaux, Y. F. Xu, Y. T. Fei, X. Y. Mo, G. X. Wang, X. S. Zhou, *Sci. Bull.* **2023**, *68*, 1819; b) D. Zhang, Y. R. Wang, Y. Yang, Y. Zhang, Y. Z. Zhao, M. Pan, Y. K. Sun, S. P. Chen, X. S. Liu, J. L. Wang, Y. N. NuLi, *Adv. Energy Mater.* **2023**, *13*, 2301795.

[9] a) D. M. Wang, X. F. Du, G. S. Chen, F. C. Song, J. H. Du, J. W. Zhao, Y. L. Ma, J. Wang, A. B. Du, Z. L. Cui, X. H. Zhou, G. L. Cui, *Angew. Chem. Int. Ed.* **2023**, *62*, e202217709; b) W. Ren, D. Wu, Y. N. NuLi, D. Zhang, Y. Yang, Y. Wang, J. Yang, J. L. Wang, *ACS Energy Lett.* **2021**, *6*, 3212.

[10] a) L. W. Wangoh, Z. Z. Yang, L. Wang, M. E. Bowden, X. M. Yin, A. T. S. Wee, K. T. Mueller, V. Murugesan, Y. G. Du, *ACS Nano* **2020**, *14*, 14887; b) X. F. Ma, H. Y. Li, X. Q. Zhu, W. W. Ren, X. Zhang, J. Diao, B. Xie, G. S. Huang, J. F. Wang, F. S. Pan, *Small* **2022**, *18*, 2202250; c) R. M. Sun, X. Ji, C. Luo, S. Hou, P. Hu, X. J. Pu, L. S. Cao, L. Q. Mai, C. S. Wang, *Small* **2020**, *16*, 2000741.

[11] a) D. Z. Wu, J. Zeng, H. M. Hua, J. N. Wu, Y. Yang, J. B. Zhao, *Nano Res.* **2020**, *13*, 335; b) H. Tang, F. Y. Xiong, Y. L. Jiang, C. Y. Pei, S. S. Tan, W. Yang, M. S. Li, Q. Y. An, L. Q. Mai, *Nano Res.* **2019**, *58*, 347; c) Y. N. Xu, X. W. Deng, Q. D. Li, G. B. Zhang, F. Y. Xiong, S. S. Tan, Q. L. Wei, J. Lu, J. T. Li, Q. Y. An, L. Q. Mai, *Chem* **2019**, *5*, 1194.

[12] C. L. Zuo, W. Tang, B. X. Lan, F. Y. Xiong, H. Tang, S. J. Dong, W. W. Zhang, C. Tang, J. T. Li, Y. S. Ruan, S. B. Xi, Q. Y. An, P. Luo, *Chem. Eng. J.* **2021**, *405*, 127005.

[13] M. Rashad, M. Asif, I. Ahmed, Z. He, L. Yin, Z. X. Wei, Y. Wang, *J. Magnesium Alloys* **2020**, *8*, 364.

[14] E. Pomerantseva, *Acc. Chem. Res.* **2023**, *56*, 13.

[15] a) Q. Zong, Y. L. Zhuang, C. F. Liu, Q. L. Kang, Y. Z. Wu, J. J. Zhang, J. Y. Wang, D. W. Tao, Q. L. Zhang, G. Z. Cao, *Adv. Energy Mater.* **2023**, *13*, 2301480; b) X. Zhao, L. Y. Li, L. R. Zheng, L. L. Fan, Y. Yi, G. B. Zhang, C. P. Han, B. H. Li, *Adv. Funct. Mater.* **2023**, 2309753.

[16] Z. Q. Wang, X. Y. Tang, S. Y. M. Bai, H. L. Wang, S. Y. Liu, M. Zhang, Y. Ma, *Adv. Funct. Mater.* **2021**, *31*, 2100164.

[17] J. Q. Zheng, C. F. Liu, M. Tian, X. X. Jia, E. P. Jahrman, G. T. Seidler, S. Q. Zhang, Y. Y. Liu, Y. F. Zhang, C. G. Meng, G. Z. Cao, *Nano Energy* **2020**, *70*, 104519.

[18] a) C. F. Liu, Z. Neale, J. Q. Zheng, X. X. Jia, J. J. Huang, M. Y. Yan, M. Tian, M. S. Wang, J. H. Yang, G. Z. Cao, *Energy Environ. Sci.* **2019**, *12*, 2273; b) X. L. Shi, Y. C. Sun, Y. B. Weng, X. Y. Long, T. X. Lei, J. L. Zhou, D. P. Li, J. Zhang, Y. Huang, L. J. Ci, K. K. Li, T. Y. Zhang, *Nano Energy* **2023**, *16*, 4670.

[19] S. Chen, K. Li, K. S. Hui, J. T. Zhang, *Adv. Funct. Mater.* **2020**, *30*, 2003890.

[20] a) L. Xu, Y. Zhang, J. Zheng, H. Jiang, T. Hu, C. Meng, *Mater. Today Energy* **2020**, *18*, 100509; b) H. B. Geng, M. Cheng, B. Wang, Y. Yang, Y. F. Zhang, C. C. Li, *Adv. Funct. Mater.* **2019**, *30*, 1907684.

[21] a) Q. Fu, A. Sarapulova, V. Trouillet, L. H. Zhu, F. Fauth, S. Mangold, E. Welter, S. Indris, M. Knapp, S. Dsoke, N. Bramnik, H. Ehrenberg, *J. Am. Chem. Soc.* **2019**, *141*, 2305; b) Y. T. Luo, Y. Bai, A. Mistry, Y. W. Zhang, D. Zhao, S. Sarkar, J. V. Handy, S. Rezaei, A. C. Chuang, L. Carrillo, K. Wiaderek, M. Pharr, K. Xie, P. P. Mukherjee, B. X. Xu, S. Banerjee, *Nat. Mater.* **2022**, *21*, 217.

[22] a) Y. J. Li, X. Feng, W. Y. Lieu, L. Fu, C. Zhang, T. Ghosh, A. Thakur, B. C. Wyatt, B. Anasori, W. Liu, Q. F. Zhang, J. Lu, Z. W. She, *Adv. Funct. Mater.* **2023**, *33*, 2303067; b) S. Z. Chang, J. B. Fang, K. Liu, Z. H. Shen, L. Zhu, X. Jin, X. J. Zhang, C. Q. Hu, H. G. Zhang, A. D. Li, *Adv. Energy Mater.* **2023**, *13*, 2204002.

[23] J. L. Hu, C. Z. Lai, K. Y. Chen, Q. P. Wu, Y. P. Gu, C. L. Wu, C. Li, *Nat. Commun.* **2022**, *13*, 7914.

[24] a) O. W. Sheng, J. H. Zheng, Z. J. Ju, C. B. Jin, Y. Wang, M. Chen, J. W. Nai, T. F. Liu, W. K. Zhang, Y. J. Liu, X. Y. Tao, *Adv. Mater.* **2020**, *32*, 2000223; b) L. E. C. Forero, P. B. Balbuena, *Phys. Chem. Chem. Phys.* **2017**, *19*, 30861; c) N. Wu, P. H. Chien, Y. M. Qian, Y. T. Li, H. H. Xu, N. S. Grundish, B. Y. Xu, H. B. Jin, Y. Y. Hu, G. H. Yu, J. B. Goodenough, *Angew. Chem. Int. Ed.* **2019**, *59*, 4131.

[25] Y. Q. Yang, Y. Tang, G. Z. Fang, L. T. Shan, J. S. Guo, W. Y. Zhang, C. Wang, L. B. Wang, J. Zhou, S. Q. Liang, *Energy Environ. Sci.* **2018**, *11*, 3157.

[26] F. Su, F. F. Xing, X. Wang, F. Y. Liu, L. Z. Zhang, Z. S. Wu, *Energy Environ. Sci.* **2023**, *16*, 222.

Manuscript received: July 26, 2024
Accepted manuscript online: August 30, 2024
Version of record online: October 25, 2024